

Sensing dot with high output swing for scalable baseband readout of spin qubits

Eugen Kammerloher,¹ Andreas Schmidbauer,² Laura Diebel,² Inga Seidler,¹ Malte Neul,¹ Matthias Künne,¹ Arne Ludwig,³ Julian Ritzmann,³ Andreas Wieck,³ Dominique Bougeard,² Lars R. Schreiber,¹ and Hendrik Bluhm¹

¹*JARA-Institute for Quantum Information, RWTH Aachen University, 52074 Aachen, Germany*

²*Fakultät für Physik, Universität Regensburg, 93040 Regensburg, Germany*

³*Applied Solid State Physics, Ruhr-Universität Bochum, 44801 Bochum, Germany*

(Dated: July 30, 2021)

A key requirement for quantum computing, in particular for a scalable quantum computing architecture, is a fast and high-fidelity qubit readout. For semiconductor based qubits, one limiting factor is the output swing of the charge sensor. We demonstrate GaAs and Si/SiGe asymmetric sensing dots (ASDs), which exceed the response of a conventional charge sensing dot by more than ten times, resulting in a boosted output swing of 3 mV. This substantially improved output signal is due to a device design with a strongly decoupled drain reservoir from the sensor dot, mitigating negative feedback effects of conventional sensors. The large output signal eases the use of very low-power readout amplifiers in close proximity to the qubit and will thus render true scalable qubit architectures with semiconductor based qubits possible in the future.

INTRODUCTION

Spin qubits based on gate-defined quantum dots (QDs), use proximal charge sensors^{1,2} and more recently dispersive gate sensing techniques³⁻⁵ for readout of the quantum state after spin-to-charge conversion.^{6,7} Proximal charge sensors can be quantum point contacts or sensing dots (SDs), of which the SD is the most sensitive sensor for spin qubit readout. Recently, the focus of new readout circuits shifts towards scalability, since high fidelity scalable readout is one of the key requirements for quantum computers with more than just a few qubits. The most widespread readout technique is based on RF reflectometry,⁸ satisfying the requirement of high fidelity, but requires bulky, power-hungry components and is not well scalable. There are solutions to miniaturize at least parts of the necessary RF equipment⁹ or use multiplexing techniques.¹⁰⁻¹² However, the overall readout complexity is not reduced significantly, since the still necessary RF components currently available do not scale well. Baseband readout, using simple transistor circuits in close proximity to the qubit, is a promising candidate for a well scalable and parallel qubit readout.¹³ Previously, single-shot readout using a HEMT amplifier was demonstrated.¹⁴ More recently, the performance was improved for amplifiers adjacent to the sample.^{13,15} Especially with the performance shown in,¹³ in principle several thousands of qubits could be read out simultaneously, within the cooling power budget of commercially available dilution refrigerators. Increasing the SD output signal would allow an even lower total power consumption, thus more simultaneous qubit readouts or a higher readout fidelity using the baseband readout approach, since the power requirement is determined by amplifier gain and sensitivity. In conventional sensing dots, however, the output swing is limited by negative feedback, due to a large drain capacitance, analogous to the Miller effect in classical electronics.¹⁶

Here, we introduce a proximal charge sensor, that uti-

lizes additional electrodes to sculpt the electrostatic potential of a SD, termed asymmetric sensing dot (ASD), that remedies this effect. We perform voltage bias transport measurements, where we observe a significant reduction in dot and drain capacitive coupling in Coulomb diamonds. We observed qualitatively similar results in remote doped GaAs/(Al,Ga)As and undoped Si/SiGe devices, supporting the universality of the concept. Also, a nearby qubit-like double quantum dot (DQD) is tuned into a multi-electron regime and the ASD is used for charge sensing. Operating the ASD in current bias mode, allows for a high voltage swing in response to a qubit charge state change, that is one to two orders of magnitude larger than previous techniques. Thus, this novel sensor design in conjunction with baseband readout may lead to a much lower power consumption charge readout or higher readout sensitivities at the same power levels, making this approach attractive for scalable quantum circuits.

ASD CONCEPT

Figure 1a depicts the electric potential of a biased SD. The ladder of QD energy levels can be shifted by the gate voltage V_G , while a bias V_D is applied to the drain D . Measuring the transport current through the device, while driving these voltages produces a characteristic diamond shaped pattern, due to Coulomb blockade effects. A section of these diamonds is depicted in the panel figure 1b, where current only flows in the gray regions. According to a constant interaction model,¹⁷ the positive and negative slopes of the Coulomb diamonds are $C_G/(C_\Sigma - C_D)$ and $-C_G/C_D$, where C_Σ is the dot's total capacitance to ground and C_G and C_D the capacitance to the swept gate electrode and drain reservoir, respectively. In the SD, the drain D is separated from the dot by a sharp tunneling barrier, that is similar to the source S , as depicted by the top sketch in figure 1b.

Using the QD for charge sensing, a nearby charge change

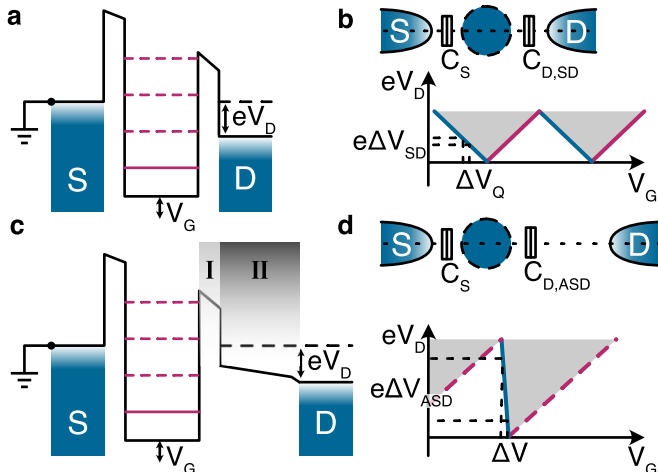


FIG. 1. Electric potential of SD and ASD and output signal. **a,c** show a schematic electric potential with an applied bias of V_D between source S and drain D for the SD and ASD, respectively. The ladder of the dots' levels can be energetically shifted by the gate voltage V_G . In the SD (panel a), the drain D is separated from the dot by a sharp tunneling barrier. In the ASD (panel b), the barrier is a compound barrier with a sharp tunnel barrier region **I** controlling tunneling and an additional intermediate barrier region **II** termed slide. **b,d** Schematic Coulomb diamonds for both sensors. There is no current flow in the white regions due to Coulomb blockade. Single-electron transport current flows in the light gray regions. Blue and red lines mark the edges of the diamond shaped Coulomb blockade regions. An equivalent shift ΔV_Q on the V_G -axis results in an enhanced shift $e\Delta V_{ASD}$ for the ASD compared to $e\Delta V_{SD}$, in current bias mode. Top insets schematically show a top-view of the potential. Source and drain electron reservoirs have a tunnel and capacitive coupling to the quantum dot (blue circle).

can be depicted on the V_G -axis as a voltage shift ΔV_Q . For a constant current bias, the resulting energy shift will be $e\Delta V_{SD}$. Typically, the resulting output voltage ΔV_{SD} is not significant, due to a large $C_{D,SD}$ and subsequently a small blue slope. In the following we will call this SD configuration conventional SD.

In figure 1c the electric potential of a biased ASD is shown. The ASD concept is to modify the drain barrier in such a way that the tunneling rate remains similar to the conventional SD, but the drain capacitance is strongly reduced to greatly increase the maximal output voltage. For this, the barrier is subdivided into a compound barrier with a sharp tunnel barrier region **I** and an additional slowly decreasing barrier region **II** termed slide. Region **II** physically separates the drain reservoir further from the dot, thus $C_{D,ASD} \ll C_{D,SD}$, while region **I** controls the tunneling at the working point. The top sketch figure 1d depicts the new SD configuration, where the asymmetric arrangement of source and drain is visible, lending itself to the name ASD. An equivalent shift ΔV_Q on the V_G -axis results now in a greatly en-

hanced shift $e\Delta V_{ASD}$ for the ASD compared to $e\Delta V_{SD}$. Thus, an important figure of merit for the ASD is the magnitude of the blue slope $-C_G/C_D$ in figure 1d, where large values indicate a higher output voltage swing of the sensor, when configured for charge sensing.

EXPERIMENTAL RESULTS

Figure 2a shows a false-colored scanning electron microscope (SEM) image of a double quantum dot (DQD) with an integrated ASD on the left side. Here, the ASD is incorporated into our GaAs qubit design, in a doped MBE-grown GaAs/(Al,Ga)As heterostructure, featuring a 2DEG 90 nm underneath the interface (details see Methods).^{18,19} The yellow colored gates DA(1-3) define a SD, while orange colored gates DA(4-6) are used to control the dot-drain transition. The purple colored gates are used to define and manipulate the nearby qubit. The source reservoir (labeled \boxtimes II) has a distance from the SD (red circle) as commonly used for conventional SDs, while the drain reservoir (\boxtimes I) is asymmetrically formed. A dashed line illustrates a possible electron trajectory connecting source and drain of the sensor. Supported by numerical electrostatic simulations, we developed device designs, where the drain barrier potential region is optimized for a slow and monotonically declining transition to the drain reservoir, in effect creating an electron slide that has a length on the μm -scale, while sharp tunnel barriers define the SD. Transport at the optimal working point is still possible, while the capacitive coupling of dot and drain is greatly reduced. To experimentally validate the ASD concept, we compare Coulomb diamonds of the sensor tuned for conventional operation with nearly symmetric source and drain barriers (gates DA(4-6) set to 0 V) in figure 2b, to a tuned up ASD in figure 2c. The sensor is operated in the multi-electron Coulomb blockade regime with a voltage bias V_D applied to ohmic contact \boxtimes II (drain), while current is measured with a transimpedance amplifier at \boxtimes I (source).

Typical values of V_D do not exceed a few hundred μV for conventional SD operation. In the following, values of V_D can easily exceed several mV, since the compound drain barrier of the ASD becomes only transparent at higher bias voltages. Figure 2b shows typical Coulomb diamonds, when operating the device in a conventional way without using the additional gate electrodes, that are symmetric around zero bias. Gate SA not only shifts the dot minimum, but also modifies the tunneling rates of the dot barriers, thus the diamond features become smeared out for higher tunneling rates at more positive voltages. At more negative voltages transport is blocked close to zero bias, as the barriers become opaque. The slope of the diamond can be evaluated at different current levels. Here we choose 100 pA, which is a compromise between low current operation and a sufficient signal-to-noise ratio. In figure 2b we fit a line at the 100 pA contour and find a maximum slope of $\beta = -0.30 \text{ V/V}$ for the SD.

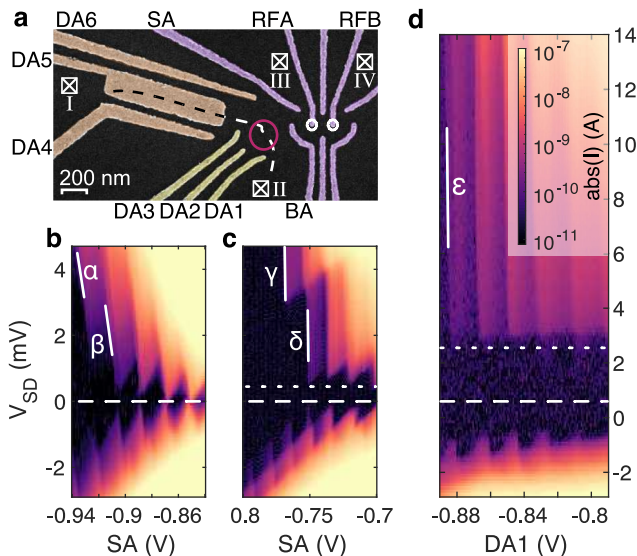


FIG. 2. Device layout and Coulomb diamond comparison in GaAs/(Al,Ga)As. **a** False-colored scanning electron micrograph (SEM) of a GaAs ASD device. Labels \boxtimes I and \boxtimes II mark the drain and source reservoirs, connected by a dashed line, corresponding to a possible electron trajectory through the sensor. A red circle marks the sensor dot position. White circles indicate the position of a DQD, which may host qubits. **b** Gate DA(4-6) are turned off (0 V) and a conventional SD with nearly symmetric source and drain reservoirs is tuned. The white dashed horizontal line indicates zero bias. White lines indicate negative slopes $\alpha = -0.25$ V/V and $\beta = -0.30$ V/V of a linear fit to the 100 pA contour. **c** The ASD is tuned up with an asymmetric source drain configuration using gates DA(4-6). The white dashed horizontal line indicates zero bias and the dotted line indicates a bias window $0 \leq V_{SD} \lesssim 360 \mu\text{V}$ with no current flow due to high drain barrier opacity. White lines indicate negative slopes $\gamma = -3.96$ V/V and $\delta = -2.29$ V/V of a linear fit to the 100 pA contour. **d** ASD Coulomb diamonds with a tuned-up nearby DQD, used later for charge sensing. Gate DA1 is used instead of SA, so as to not miss-tune the DQD, which is less sensitive to this gate electrode. The white dashed horizontal line indicates zero bias and the dotted line indicates a bias window $0 \leq V_{SD} \lesssim 2.9$ mV with no current flow.

Note, that for a conventional SD the slope remains nearly constant even at higher bias values.

Figure 2c shows equivalent measurements with the sensor tuned to the ASD regime. The Coulomb diamonds change distinctively from the conventional case and the positive and negative bias configurations are not symmetric any more. A bias dependence of the Coulomb lines is observed for slopes γ and δ of the ASD, compared to α and β for the SD. At higher bias, a maximal slope of $\gamma = -3.96$ V/V at the 100 pA contour is observed²⁰. The steepening of Coulomb diamonds indicates the desired reduction of C_D by a factor of $C_{D,SD}/C_{D,ASD} \approx 13$, compared to the maximal slope in figure 2b. Additionally, we observe a bias window in figure 2c, where transport is blocked ($0 \leq V_{SD} \leq V_T$, where $V_T \lesssim 360 \mu\text{V}$), in between

the dashed and dotted white lines. We find in figure 2d that when a nearby qubit-like DQD is also tuned up, V_T can be of the order of several mV, which results in low visibility of the typical Coulomb blockade features near zero bias. Further details of ASD tuning are discussed in the Methods section.

To test the adaptability of our ASD concept, we also realized a device in a MBE-grown Si/SiGe heterostructure, featuring a 10 nm thick Si QW separated from the interface by a 35 nm thick Si₆₅Ge₃₅ spacer (details see Methods). Transferring the ASD from a remote-doped GaAs to an undoped Si/SiGe heterostructure requires a full redesign of the gate pattern: First, Si/SiGe requires an accumulation gate also above the slide region and second the gate pattern has to be shrunk down to compensate for the three times larger effective electron mass. Therefore, we implemented a new simulation-guided design to host the ASD and a nearby DQD. A false-colored SEM image of this gate layout is shown in figure 3a. The sensor dot is formed by the light yellow colored gates, from which gate PS serves as the plunger gate for the sensor quantum dot levels. Gates SL, SR and ST (colored orange) form the potential slide (region II in figure 1c) and the purple colored gates may be used to tune two tunnel-coupled QDs in the vicinity of the sensor dot. Current through the sensor is defined by ohmic contacts \boxtimes I and \boxtimes II, while contacts \boxtimes III and \boxtimes IV serve as electron reservoirs for the DQD. Tuning the electrostatic potential to form a sensor QD below gate PS, we record a series of Coulomb blockade measurements to test the tunability of the slide potential region II. Starting from a conventional symmetric configuration in figure 3b, the slide is then activated by only reducing the voltage on gate SR, while simultaneously increasing the voltage on gate BLS to retain the same tunnel rate (keep region I in figure 1b constant) for transport through the sensor: In figure 3b-d, we decreased the voltage on gate SR from 0.34 V to 0.24 V and 0.215 V, respectively. Similar to the observation in GaAs, for the most negative SR configuration a blockade region with a threshold voltage of $V_T = 1$ mV emerges²¹.

The series in figure 3b-d clearly shows that the negative Coulomb diamond edges become steeper, the smaller the voltage applied to the gate SR. For all three diamonds shown here, we determined these negative Coulomb diamond slopes, by fitting the 50 pA contour, which represents the best compromise between a low-current operation of the device and a sufficient signal-to-noise ratio. The slopes in figure 3b-d represent the steepest slopes which we found for each configuration²². Starting from $\alpha = -0.68$ V/V for the most symmetric configuration, we reach $\beta = -3.2$ V/V for the intermediate configuration and finally $\gamma = -8.0$ V/V for the most asymmetric configuration, corresponding to a twelve-fold reduction of $C_{D,ASD}$.

Hence, we have shown that the ASD concept is equally efficient across material platforms. Integrating ASDs into a DQD environment, we have demonstrated a control-

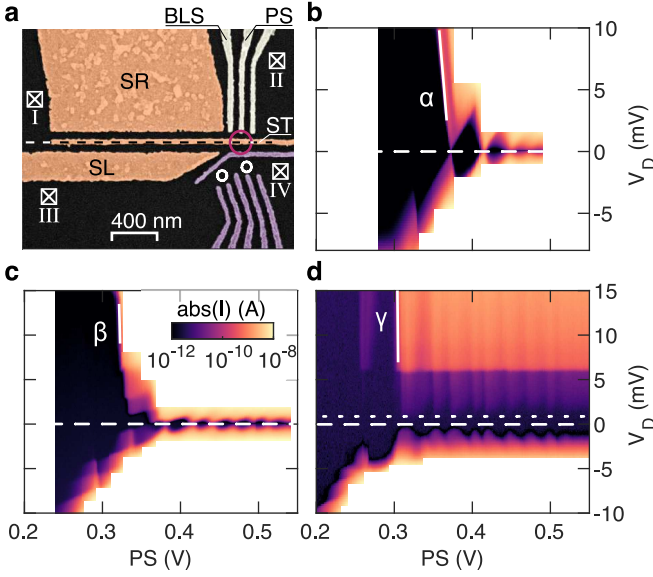


FIG. 3. Device layout and Coulomb diamond comparison in Si/SiGe. **a** False-colored SEM image of an ASD device in Si/SiGe similar to the one measured. A global top-gate isolated by Al_2O_3 is not shown. The light yellow colored gates (including BLS and PS) define the sensor QD in vicinity to the purple colored gates, which can be used to form a DQD. The potential slide for the ASD operation of the SD is formed by the orange colored gates (SR, SL and ST). The drain and source reservoirs are labeled \boxtimes I and \boxtimes II for the sensor current path and \boxtimes III and \boxtimes IV for the DQD current path. **b-d** Coulomb diamond measurement series tuning the SD from a symmetric to an asymmetric configuration. To do so the gate potential of SR is step-wise decreased from 0.34 V in (b) to 0.24 V in (c) to 0.215 V in (d) and simultaneously the gate potential of BLS is adjusted to maintain the same tunnel rate for transport through the SD. The measurements are performed by varying the drain potential V_D at the reservoir \boxtimes I while keeping the reservoir \boxtimes II at zero volt for different potentials at PS, which serves as plunger gate for the sensor quantum dot levels. The white lines indicate the negative slopes of the corresponding Coulomb diamonds. Linearly fitting the 50 pA contour leads to slopes of $\alpha = -0.68 \text{ V/V}$ for (a), $\beta = -3.2 \text{ V/V}$ for (b) and $\gamma = -8.0 \text{ V/V}$ for (d).

lable reduction of $C_{D,ASD}$ both in Si/SiGe and GaAs while being able to maintain a tunneling rate useful for operation of the sensor quantum dot. In the proof-of-principle experiments discussed in figures 2 and 3, we reached a maximal reduction of $C_{D,ASD}$ by a factor of 13 in GaAs and a factor of 12 in Si/SiGe, implying an increase by the same factor of the voltage swings produced by these ASDs, compared to conventional sensor dots.

In figure 4, we discuss several features of the ASD Coulomb diamonds in more detail. We focus on $V_D > 0$, since the ASD has a preferential bias direction and the behavior for $V_D < 0$ is unimportant for the intended mode of operation. Regions in the Coulomb diamond plot where transport is possible, are colored in gray. The blue slope is the desired working point for readout and

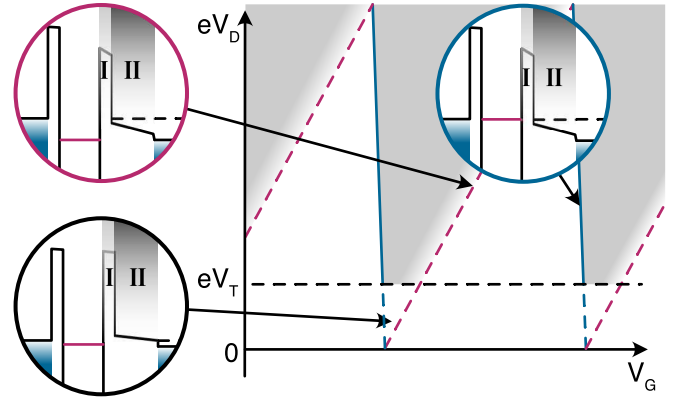


FIG. 4. ASD Coulomb diamond details. Schematic of Coulomb diamonds expected for the ASD. Single electron current flows in the light gray regions separated by a blue solid line and red dashed line from Coulomb blockade regions (white). The white current-free region is extended by the threshold voltage V_T (black dashed line). Three insets in black, red and blue frames, depict details of the ASD potential at the corresponding (V_G, V_D) operation points marked by arrows.

the corresponding chemical potentials of the reservoirs and last occupied energy level of the QD are depicted in the blue inset. The red energy level in the QD is close to the chemical potential of the source. Tunneling through the thin barrier I is possible at sufficiently high bias, after which the electron passes through region II and relaxes down into the drain reservoir. Along the opposing diamond edge, the energy level in the dot is close to the chemical potential of the drain, as illustrated in the red inset. However, tunneling through barrier I in addition to barrier II becomes exponentially difficult, hence current flow degrades when approaching the dashed red slope from the left. Note, that for our device configurations tuned into the ASD regime, such as figure 2d and figure 3d, we observe that the positive slopes, also indicated as red dashed lines in the schematic in figure 1c, are indeed fading. The black inset depicts low bias configurations, below the dashed black line. The inset shows a state where the dot energy level is inside the bias window and can potentially contribute to the current flow, however tunneling is nearly impossible, due to the combined barrier thickness of regions I-II. The compound drain barrier is only transparent above a threshold V_T , when a sufficiently large gradient is formed in region II by the bias voltage. Since the ASD compound drain barrier is exceedingly sensitive to gate voltage changes on nearby structures, compensation for these changes can reduce the operational bias voltage space to even higher values of V_T . Additionally, any disorder effects that create local minima in region II, may result in an even higher value of V_T to compensate.

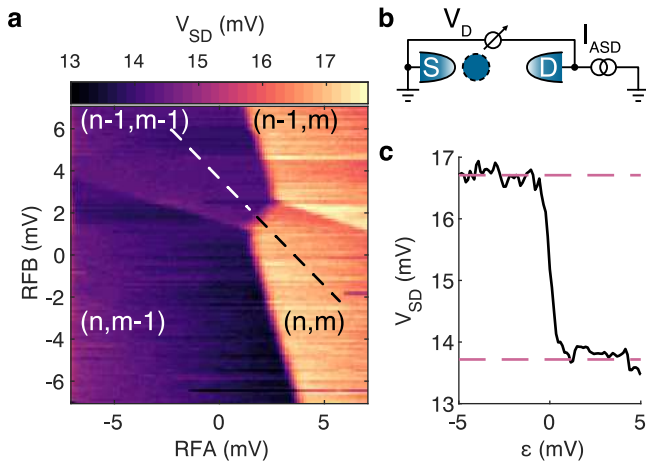


FIG. 5. **Charge sensing with current biased ASD.** **a** The ASD is configured for charge sensing of a nearby multi-electron DQD with a $I_{ASD} = 500$ pA current bias. The charge stability diagram is recorded with the ASD, using the voltage drop V_D across the sensor as the signal (median adjustment per scan-line). **b** Schematic of the ASD wiring. **c** Cut on the detuning axis ϵ , corresponding to the dashed line on the left panel (linear background subtracted). A voltage swing of 3 mV is observed.

ASD CHARGE SENSING

To demonstrate charge sensing operation with the ASD, we define a qubit-like DQD in the center of the GaAs device, by employing the purple colored gates in figure 2. When operated as a charge sensor, it is necessary to reconfigure the ASD for current bias, to benefit from the high output voltage swing. Here, a constant current source supplies 500 pA through the drain, while the source is grounded. We tune the ASD to a sensitive position and record a charge stability diagram of the DQD using gates RFA and RFB in figure 5a (see section Methods for tuning details). The voltage drop V_D across the ASD is monitored with a voltmeter (see figure 5b). Figure 5c shows the voltage swing across the inter-dot transition of the DQD (dashed line in figure 5a), corresponding to a qubit state change. We observe a voltage swing of 3 mV. We expect the voltage swing to be one order of magnitude larger than a conventional SD in this configuration, due to the one order of magnitude difference in slopes β and γ in figure 2, which give a measure of sensor sensitivity, as discussed in figure 1c-d.

DISCUSSION

In conclusion, we have demonstrated a new type of proximal charge sensor capable of more than ten times the previous output voltage. The drain capacitance was reduced by a factor of 12 and 13 respectively, compared to a normal SD in both undoped Si/SiGe and doped GaAs devices, supporting the adaptability of our ASD concept

across different material systems. In further experiments it would be interesting to determine, how strong the ASD disturbs the host qubit, due to the higher energy electrons produced during sensor operation compared to conventional SDs.^{23,24}

Also, compared to the conventional SD, the ASD has a much larger small-signal output resistance r_{ASD} , due to the intended weak dependence of the current on the output voltage. Thus, the time constant $\tau = r_{ASD}C_P$ associated with reaching the steady state level of the output swing can be much longer than in conventional SDs. Here C_P corresponds to the sum of the subsequent amplifier input capacitance and other parasitic capacitances. During readout, C_P is linearly charged. However, it is not necessarily important to wait for the saturation. After the readout, C_P can be reset by tuning the ASD into a lower resistance regime or possibly an active reset by a bypass transistor, thus having a high small-signal output resistance is not harmful. In this case, the accessible output voltage is limited by the charging of C_P . Thus, it is essential to minimize C_P as much as possible, to benefit from a large output voltage swing for transient, qubit lifetime-limited signals. For a typical current change of $i_{ASD} = 200$ pA during charge sensing, reaching a $V_1 = 3$ mV swing in $t_1 = 1 \mu\text{s}$ corresponds to a capacitance value of $C_P = t_1 i_{ASD} / V_1 \approx 67$ aF. This should be achievable with unpackaged optimized transistors without ESD protection a few hundred μm from the qubit. Further reductions may be possible with techniques like flip-chip bonding. Using baseband transistor readout in close proximity to the ASD for optimal C_P as in,¹³ promises a well scalable solution in terms of footprint and power consumption. Earlier work using HEMT/HBTs suggests a power requirement as low as 800 nW for amplifiers adjacent to the sample.¹³⁻¹⁵ Using the ASD with a ten times larger output signal, ten to a hundred thousand qubits could be read out in parallel, without any multiplexing, within the cooling power budget of commercially available dilution refrigerators.

METHODS

GaAs/(Al,Ga)As and Si/SiGe heterostructure

The GaAs/(Al,Ga)As device was fabricated on a MBE-grown heterostructure (sample B14722). The layer stack is grown at a constant temperature of 695 °C. A 35 nm $\text{Al}_{0.65}\text{Ga}_{0.35}\text{As}$ layer is grown on the GaAs substrate, followed by an additional 50 nm Si modulation doped $\text{Al}_{0.65}\text{Ga}_{0.35}\text{As}$ layer. A 5 nm Si doped GaAs cap finalizes the structure, thus the 2DEG is formed 90 nm below the interface. The ohmic contacts to the 2DEG are thermally activated by a rapid anneal at 460 °C of a gold/germanium alloy. The mobility of the 2DEG, as obtained by Hall measurements at a temperature of 4.2 K, is of the order of $1.47 \times 10^6 \text{ cm}^2/(\text{Vs})$ at an electron density of $1.82 \times 10^{11} \text{ cm}^{-2}$. A single layer of metal gates is

fabricated by means of electron beam lithography.

The Si/SiGe device was fabricated on a solid-source MBE-grown heterostructure. A relaxed virtual substrate consists of a graded buffer grown at 500 °C up to a composition of $\text{Si}_{0.65}\text{Ge}_{0.35}$ on a Si substrate without intentional miscut and a layer of constant composition $\text{Si}_{0.65}\text{Ge}_{0.35}$. It provides the basis for a 10 nm natural Si QW grown at a substrate temperature of 350 °C. The QW is separated from the interface by 35 nm $\text{Si}_{0.65}\text{Ge}_{0.35}$. The structure is protected by a 1.0 nm naturally oxidized Si cap. The implanted ohmic contacts to the QW are thermally activated by a rapid anneal at 700 °C. The mobility of the 2DEG formed in the QW, as obtained by Hall measurements at a temperature of 1.5 K, is of the order of $1.1 \times 10^6 \text{ cm}^2/(\text{Vs})$ at an electron density of $6.6 \times 10^{11} \text{ cm}^{-2}$ and is limited by remote impurity scattering.²⁵ A 10 nm layer of Al_2O_3 grown by atomic layer deposition insulates the first metal gate layer and the underlying heterostructure. The metal gates are fabricated by means of electron beam lithography. A second gate layer, insulated from the first gates by 50 nm of Al_2O_3 , is used to induce a two-dimensional electron gas in the QW via the field effect. A Co magnet is deposited on top of the device. Bias-cooling using voltages of -0.5 V at the gates of the first metal layer and -4.8 V applied to global gate of the second metal layer, is employed for the Si/SiGe devices from room temperature to 300 mK, to inhibit leakage between the gate layers.

ASD Tuning

The ASD can be tuned under voltage or current bias. Tuning under voltage bias involves slope evaluation of Coulomb diamond features, to find the desired regime. Tuning under current bias is closer to the intended mode of operation and lends itself for routine use and automation, since the output voltage swing can be directly measured and easily optimized by a parameter sweep.

In the following, the tuning of the GaAs device is discussed under voltage bias initially. For an untuned device, gate electrodes SA and BA should be set below their pinch-off value and provide a fixed barrier, so current can only flow from $\boxtimes\text{I}$ to $\boxtimes\text{II}$. Gate DA6 is set to the same voltage as gate SA, and can be used later, for fine-tuning the sensor and compensate for unrelated tuning operations performed on the nearby qubit. A useful starting point for ASD tuning, is the slide gate electrode (DA5) versus slide barrier gate electrodes (DA3 and DA4, while DA6 is kept fixed) diagram in figure 6. Two parallel conducting channels are observed. Conduction below DA5 (marked with II) and undesired leakage below DA3 or DA4 far away from the ASD (III). The dashed lines represent the conduction onset for these channels. Gate voltages marked with a white star provide starting values for DA(3-5), when tuning the ASD. Here, the lever arms of DA(3-5) are similar, indicating a barrier formation close to the desired first sensor barrier between DA3

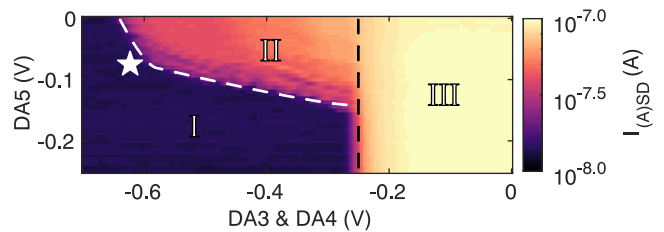


FIG. 6. **Slide gate vs. barriers diagram.** This measurement reveals several distinct features in a voltage bias ($V_D = 100 \mu\text{V}$) measurement by sweeping gates DA(3-5). Region III, at voltages where the barriers do not suppress the 2DEG below the gates is undesired leakage. Region II, where a channel exists below DA5. Some line structure can be observed, indicating a disorder dot situated in the channel. In region I, current flow is fully suppressed. A white star marks a useful voltage starting point for tuning.

and DA6. Some line structure can be observed, indicating a disorder dot situated in the channel. Simulations suggest, that a dot can arise between DA5 and DA3, at certain gate voltage combinations, even without an additional disorder potential, due to the gate geometry. The second sensor barrier is defined in the following step.

Sweeping DA1 versus DA3 reveals Coulomb lines of the sensing dot (figure 7a,b). At a low voltage bias of $V_D = 100 \mu\text{V}$ in figure 7a, the sensor has a disorder dot in series, which further modulates the Coulomb blockade. Raising the bias voltage to 1 mV in figure 7b, nearly suppresses the disorder dot. The strong influence of V_D indicates the disorder dot's position to be in the channel below DA5 or between DA5 and DA3. To further tune the sensor under voltage bias mode, we measure Coulomb diamonds. The negative diamond slope can be evaluated and optimized for a higher magnitude at different settings of DA(1-6) (similar to figure 2). However, finding suitable gate voltages is a very device layout specific process, due to the strong capacitive interdependence of the sensor gates and may require several parameter sweeps, while evaluating line features in Coulomb diamond plots at each iteration. In the following, the sensor is tuned further in current bias mode, which is the more expedient approach.

The sensor is now reconfigured for current bias of $I_{ASD} = 500 \text{ pA}$ with an voltage compliance of $V_D \leq 50 \text{ mV}$ and the same parameters otherwise (see also figure 5b for a schematic). In figure 7c the voltage drop across the sensor is depicted. The voltage drop is of the order of tens of mV for this sensor configuration and saturates at the compliance value below the dashed line, when transport is fully blocked. The derivative in sweep-direction in figure 7d reveals a structure, similar to the Coulomb lines in figure 7b, where slope β is similar to δ . Gate DA3 has a strong influence on the transport, since it controls the compound drain barrier. We observe regions of maximum voltage swing close to the full blockade (one such region marked with white cross), which is

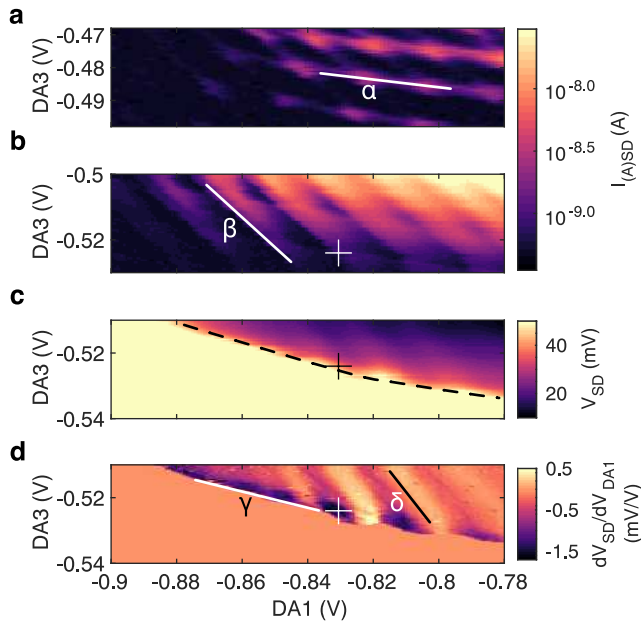


FIG. 7. **Sensor wall to wall diagrams.** **a** At a voltage bias of $V_D = 100 \mu\text{V}$, the sensor dot has a disorder dot in series, which further modulates the current Coulomb blockade. Slope α is -0.13 V/V . **b** At a voltage bias of $V_D = 1 \text{ mV}$, the disorder dot is nearly suppressed, revealing the sensor's Coulomb lines. Slope β is -0.95 V/V . **c,d** Sensor is reconfigured for current bias of $I_{ASD} = 500 \text{ pA}$ and $V_D \leq 50 \text{ mV}$ compliance, with an otherwise unchanged gate voltage configuration. **d** The derivative in sweep-direction reveals the Coulomb line structure and areas with large voltage swing. The maximum voltage swing is marked with a cross. Slope γ and δ are -0.26 V/V and -1.10 V/V .

the desired working point of the ASD for charge sensing. Voltage changes on nearby structures can shift the working point and can require compensation on the ASD gates, since the sensitive regions are small in extent.

DATA AVAILABILITY

The data sets generated and/or analyzed during this study are available from the corresponding author upon reasonable request.

ACKNOWLEDGEMENTS

This work was funded by ARO under the contract NO W911NF-17-1-0349 titled "A scalable and high performance approach to readout of silicon qubits" and by the German Research Foundation (DFG) within the project BO 3140/4-1. The device fabrication has been done at HNF - Helmholtz Nano Facility, Research Center Juelich GmbH.²⁶

COMPETING INTERESTS

The authors declare no competing interests.

AUTHOR CONTRIBUTIONS

The study was conceived by H.B. L.R.S. and D.B. The GaAs heterostructures were prepared by J.R. A.L. and A.W. and sample fabrication performed by M.K. E.K. conducted the experiments data analysis and numerical simulations on the GaAs samples, advised by H.B. The Si/SiGe heterostructures were prepared by D.B. Numerical simulations, the device design and the sample fabrication for Si/SiGe was performed by I.S. M.N. and L.R.S. A.S. L.D. and D.B. conducted the experiments and the data analysis on the Si/SiGe samples. All authors discussed the results. E.K. A.S. L.D. D.B. L.R.S. and H.B. wrote the manuscript.

1. M. Field, C. G. Smith, M. Pepper, D. A. Ritchie, J. E. Frost, G. A. Jones, and D. G. Hasko, *Physical Review Letters* **70**, 1311 (1993).
2. R. J. Schoelkopf, P. Wahlgren, A. A. Kozhevnikov, P. Delsing, and D. E. Prober, *Science* **280**, 1238 (1998).
3. J. I. Colless, A. C. Mahoney, J. M. Hornibrook, A. C. Doherty, H. Lu, A. C. Gossard, and D. J. Reilly, *Physical Review Letters* **110**, 1 (2013).
4. A. West, B. Hensen, A. Jouan, T. Tanttu, C. H. Yang, A. Rossi, M. F. Gonzalez-Zalba, F. E. Hudson, A. Morello, D. J. Reilly, and A. S. Dzurak, *Gate-based single-shot readout of spins in silicon*, Tech. Rep. (2018).
5. G. Zheng, N. Samkharadze, M. L. Noordam, N. Kalhor, D. Brousse, A. Sammak, G. Scappucci, and L. M. K. Vandersypen, *Rapid high-fidelity gate-based spin readout in silicon*, Tech. Rep. (2019).
6. L. H. Willems van Beveren, S. Tarucha, J. M. Elzerman, J. S. Greidanus, R. Hanson, S. De Franceschi, L. M. Vandersypen, L. P. Kouwenhoven, S. De Franceschi, L. M. Vandersypen, S. De Franceschi, and L. M. Vandersypen, *Physical Review B - Condensed Matter and Materials Physics* **67**, 161308 (2003).
7. A. C. Johnson, J. R. Petta, C. M. Marcus, M. P. Hanson, and A. C. Gossard, *Physical Review B - Condensed Matter and Materials Physics* **72**, 1 (2005).
8. D. J. Reilly, C. M. Marcus, M. P. Hanson, and A. C. Gossard, *Applied Physics Letters* **91**, 162101 (2007).
9. A. C. Mahoney, J. I. Colless, S. J. Pauka, J. M. Hornibrook, J. D. Watson, G. C. Gardner, M. J. Manfra, A. C. Doherty, and D. J. Reilly, *Physical Review X* **7** (2017).
10. J. M. Hornibrook, J. I. Colless, A. C. Mahoney, X. G. Croot, S. Blanvillain, H. Lu, A. C. Gossard, and D. J. Reilly, *Applied Physics Letters* **104**, 103108 (2014).
11. J. M. Hornibrook, J. I. Colless, I. D. Conway Lamb, S. J. Pauka, H. Lu, A. C. Gossard, J. D. Watson, G. C. Gardner, S. Fallahi, M. J. Manfra, and D. J. Reilly, *Physical*

- Review Applied **3**, 1 (2015).
12. S. Schaal, S. Barraud, J. J. Morton, and M. F. Gonzalez-Zalba, *Physical Review Applied* **9**, 54016 (2018).
 13. M. J. Curry, M. Rudolph, T. D. England, A. M. Mounce, R. M. Jock, C. Bureau-Oxton, P. Harvey-Collard, P. A. Sharma, J. M. Anderson, D. M. Campbell, J. R. Wendt, D. R. Ward, S. M. Carr, M. P. Lilly, and M. S. Carroll, *Scientific Reports* **9**, 1 (2019).
 14. I. T. Vink, T. Nooitgedagt, R. N. Schouten, L. M. K. Vandersypen, and W. Wegscheider, *Applied Physics Letters* **91**, 23 (2007).
 15. L. A. Tracy, D. R. Luhman, S. M. Carr, N. C. Bishop, G. A. Ten Eyck, T. Pluym, J. R. Wendt, M. P. Lilly, and M. S. Carroll, *Applied Physics Letters* **108**, 63101 (2016).
 16. P. Horowitz and W. Hill, *The Art of Electronics*, 3rd ed. (Cambridge University Press, New York, NY, USA, 2015).
 17. R. Hanson, J. R. Petta, S. Tarucha, and L. M. K. Vandersypen, *Reviews of Modern Physics* **79**, 1217 (2007).
 18. S. J. Macleod, A. M. See, A. R. Hamilton, I. Farrer, D. A. Ritchie, J. Ritzmann, A. Ludwig, and A. D. Wieck, *Applied Physics Letters* **106** (2015).
 19. P. Cerfontaine, T. Botzem, J. Ritzmann, S. S. Humpohl, A. Ludwig, D. Schuh, D. Bougeard, A. D. Wieck, and H. Bluhm, *Nature Communications* **11**, 5 (2020).
 20. On a side note: Since $dV_{SD}/dV_{SA} > 1$, the ASD has voltage gain and can be used as an ultra low-power, low stray capacitance voltage amplifier in principle, with the limitation of a narrow dynamics range.
 21. Even lower voltages on SR led to yet higher V_T .
 22. Interpolation of the data sets along the plunger gate (PS) direction was used to compensate for the lower measurement resolution on this gate.
 23. G. Granger, D. Taubert, C. E. Young, L. Gaudreau, A. Kam, S. A. Studenikin, P. Zawadzki, D. Harbusch, D. Schuh, W. Wegscheider, Z. R. Wasilewski, A. A. Clerk, S. Ludwig, and A. S. Sachrajda, *Nature Physics* **8**, 522 (2012).
 24. D. Harbusch, D. Taubert, H. P. Tranitz, W. Wegscheider, and S. Ludwig, *Physical Review Letters* **104**, 196801 (2010).
 25. A. Wild, J. Kierig, J. Sailer, J. W. Ager, E. E. Haller, G. Abstreiter, S. Ludwig, and D. Bougeard, *Applied Physics Letters* **100**, 1 (2012).
 26. W. Albrecht, J. Moers, and B. Hermanns, *Journal of large-scale research facilities JLSRF* **3**, A112 (2017).